

MOCLIP: A Foundation Model for Large-Scale Nanophotonic Inverse Design

S. Rodionov^{1†}, A. Burguete-Lopez^{1†}, M. Makarenko¹, Q. Wang¹, F. Getman¹, & A. Fratalocchi^{1*}

¹PRIMALIGHT, Faculty of Electrical Engineering; Applied Mathematics and Computational Science, King Abdullah University of Science and Technology, Thuwal 23955-6900, Saudi Arabia

[†] First author with equal contribution.

* Corresponding author. email: andrea.fratalocchi@kaust.edu.sa.

Foundation models (FM) are transforming artificial intelligence by enabling generalizable, data-efficient solutions across different domains for a broad range of applications. To date, the lack of large and diverse datasets challenges the development of FM in nanophotonics. This work presents MOCLIP (Metasurface Optics Contrastive Learning Pretrained), a nanophotonic foundation model that integrates metasurfaces' structural and spectral information in a shared latent space. MOCLIP employs contrastive learning to align geometries and spectra latent vectors on an experimentally acquired dataset equivalent in sample density to ImageNet-1K, one of the most popular datasets in machine vision used to train the latest generation of transformers for imaging tasks. The study demonstrates MOCLIP's inverse design capabilities for high-throughput zero-shot prediction at a rate of $2 \cdot 10^5$ samples per second, designing an entire 4-inch wafer filled with high-density metasurfaces in minutes, and generative latent space optimization reaching 97% accuracy. It also introduces a concept of optical information storage technology that leverages MOCLIP to achieve a storage den-

sity of 0.1 Gbit/mm² at the resolution limit, surpassing commercial optical media by a factor of six. These results position MOCLIP as a scalable, versatile platform for next-generation photonic design and data-driven applications.

Introduction

Deep learning has rapidly permeated nanophotonic inverse design, enabling advancements in metasurfaces [1–6], photonic crystals [7], plasmonics [8], and photonic integrated circuits [9]. Deep neural networks open up applications in Tb/s hyperspectral video understanding [10], computational imaging [11], and optical sensing [12]. The next frontier in the field involves integrating artificial general intelligence (AGI) concepts to bridge the gap between data-driven science and physical design constraints, and to discover new forms of adaptive photonics solutions [3, 13].

The latest advancements in AGI, represented by foundation models (FMs) [14–16], currently drive innovation across multiple scientific fields, including machine vision [17], medical diagnosis [18–20], climate modeling [21], material chemistry [22, 23], and robotics [24]. In nanophotonics, FMs could transform inverse design from bespoke, task-specific optimization, and deep learning pipelines into unified representations that generalize across devices, facilitating automated design and data-driven analysis of increasingly complex nanophotonic architectures [3].

A primary hurdle to implementing FMs in nanophotonics is their substantial training data requirement [25]. Robust generalization performance demands high dataset variability, quantified by the number of degrees of freedom (DOFs) of the nanostructures [26–28], or equivalently by the in-

trinsic dimension (ID) of the data manifold [28, 29]. The relationship between the dataset size N required to train a deep learning model efficiently and the DOFs d follows the power law $N = kd^\alpha$, where k is a constant and α ranges approximately between 0.1 and 2 depending on the modality and task [27, 30–32]. Figure 1 compares the state-of-the-art nanophotonic and computer vision datasets based on their size and DOFs. Computer vision datasets, such as ImageNet-1K, used to train the latest generation of FM transformers, exhibit DOFs of approximately 40, yielding densities of 30 000 samples per DOF [27]. In contrast, nanophotonic datasets typically have fewer than 10 DOFs and contain about 10 to 1000 samples per DOF [33–39], resulting in sample densities per DOF that require orders of magnitude enhancements to reach FM standards [16]. The difficulty in increasing the scale and diversity of nanophotonic datasets stems from the reliance on computationally intensive electrodynamic simulations [1, 25]. Simulations generate approximately one sample per minute, even when conducted on high-performance computing platforms (e.g., FDTD on an HPE Cray EX supercomputer using 192 cores). Apart from their slow data generation rate, simulations often fail to accurately capture real material properties, structural imperfections, and rarely model response deviations from the plane-wave approximation [6, 25], limiting the generalization properties of deep learning models trained using simulated data.

This work introduces an FM for nanophotonic inverse design named Metasurface Optics Contrastive Learning Pretrained (MOCLIP). The model uses more than 11 000 samples per DOF, exceeding the density of most state-of-the-art computer vision datasets and approaching the scale of ImageNet-1K. MOCLIP generalizes the Contrastive Language-Image Pretrained (CLIP) model [40], originally developed by OpenAI for computer vision and widely used in applications such as Sta-

ble Diffusion [41], to the domain of nanophotonics. MOCLIP provides a unified embedding space for metasurface geometries and their spectral responses, enabling both spectrum-to-geometry retrieval (inverse design) and geometry-to-spectrum retrieval (spectra prediction) [42] within a single framework.

MOCLIP undergoes training entirely on experimental data, without resorting to computer simulations, using a dataset generation strategy that combines dense wafer-scale fabrication with automated hyperspectral (HS) measurements. The process enables manufacturing around 40 samples per minute and their optical characterization at a rate of 380 samples per minute. This work showcases different applications of MOCLIP, including large-scale inverse design via zero-shot prediction at a rate of $2 \cdot 10^5$ samples per second, generative latent space optimization for high-fidelity inverse design with over 97% accuracy, and a proof-of-concept optical memory storage technology with information density up to 0.1 Gbit/mm^2 , enhancing the information density of commercial optical solutions by a factor of six [43].

Results

Figure 2 summarizes MOCLIP’s dataset generation, high-level architecture, and applications. Dataset generation starts by algorithmically generating a library of random free-form metasurface geometries from shape primitives represented by ellipses, rectangles, and rings (Fig. 2a). Subsequent fabrication implements these patterns into silicon-on-glass metasurfaces, producing multiple geometries on a single substrate. A custom-made automated hyperspectral transmission microscope

measures each metasurface (Fig. 2b). Figure 2c illustrates the measurement results, comprising a collection of spectral responses for every metasurface geometry. The union of all metasurface geometries and their corresponding spectral responses comprises MOCLIP’s training dataset.

Following the CLIP FM architecture, the framework trains two distinct encoders with input data pairs comprising experimental spectral response curves and binary geometry images (Fig. 2d-e).

MOCLIP uses a multilayer perceptron (MLP) encoder architecture for the spectral response curves, and a convolutional neural network (CNN) encoder architecture for the images. The model embeds the encoder’s output into a shared low-dimensional latent space (Fig. 2f). MOCLIP’s training aligns the embeddings of matching geometry (A) and spectra (B) pairs by maximizing the cosine similarity S_C between their latent vectors, while simultaneously minimizing the similarity between all non-matching (off-diagonal) pairs:

$$S_C(\mathbf{A}, \mathbf{B}) = \frac{\mathbf{A} \cdot \mathbf{B}}{\|\mathbf{A}\| \|\mathbf{B}\|} \quad (1)$$

Once trained, MOCLIP readily adapts to a broad range of applications in inverse design, including zero-shot prediction, generative latent space optimization, and automated optical information encoding and storage – all with zero to minimal fine-tuning (Fig. 2g-i).

Dataset generation

Dataset generation starts with a stochastic approach that randomly combines shape primitives to generate free-form design geometries (see Methods). The generation algorithm enforces dimensional limits and verifies element placement to ensure compliance with the fabrication process tolerances. Metasurface fabrication involves electron beam lithography patterning amorphous silicon layers on fused silica substrates (see Methods). Figure 3a shows a set of fabricated samples, each containing six metasurface arrays, integrating over 130 000 individual metasurfaces per substrate. Figures 3b-d present scanning electron microscope (SEM) images showing examples of the fabricated metasurface arrays for different geometries. Each metasurface covers a 6 μm sided square in its array. Quality assessment of the experimental samples involves fabricating a companion 10 \times 10 metasurface array containing randomly sampled entries for each of the 24 arrays. SEM characterization of these companion arrays reveals a mean size difference and standard deviation of 4 nm and 10 nm, respectively, between the fabricated structures and their designs across all dataset’s metasurfaces. Manufacturing a replicated dataset containing identical copies of the 24 arrays’ geometries arranged in a different order accounts for fabrication artifacts, contamination, and neighboring structures’ crosstalk, allowing for metasurface response cross-validation in MO-CLIP.

Figure 3e illustrates the hyperspectral transmission microscope setup used to characterize the metasurfaces’ optical responses. A broadband light beam generated by a light source (LS) passes through a collimating lens (L), a polarizer (POL), and a tunable filter (TF), forming a monochro-

matic beam of tunable wavelength and controlled linear polarization. A half-wave plate (HWP) controls the polarization of the filter output, after which a series of mirrors (M) and lenses direct the light through the microscope's aperture and field stops (AS, FS), focusing it onto the back focal plane of an objective (OBJ) to illuminate the sample with Köhler illumination. A second objective and a tube lens (TL) image the sample in transmission with a camera (CAM). Simultaneously, the setup diverts a portion of the beam using a beam splitter (BS) to a reference camera (RCAM), which monitors and compensates for intensity fluctuations.

For each array, the setup records two stacks of narrow-band images by driving the TF from 450 nm to 730 nm in 10 nm increments at its minimum bandwidth setting (10 nm) for x and y polarization, generating two hypercubes per array. The Supplementary Materials provide detailed information on the setup components and measurement error analysis. Figure 3f shows a representative hyperspectral datacube acquired from a single metasurface array under fixed polarization conditions. False colors enhance visualization, with the dark rectangular region at the center corresponding to the spatial footprint of the array. Figure 3g provides an expanded view of the metasurface array structures under broadband illumination, showing the spectral response of each metasurface captured by a conventional red, green, and blue (RGB) camera as different colors. Figure 3h depicts the response of a typical metasurface computed from the hypercube's pixel values. The green and blue lines represent the readings obtained from all pixels covering a single metasurface in the x and y polarization hypercubes; the black and orange lines show the averaged pixel responses used as dataset entries. Cross-validation of every metasurface spectrum with that of its corresponding duplicate in the replicated dataset ensures quality by discarding entries with a mean-squared error

(MSE) difference exceeding the 10^{-3} value, resulting in a dataset of 466 537 unique metasurface geometry-spectra pairs.

MOCLIP training

Figure 4 illustrates MOCLIP’s training process. The pipeline follows a two-modality contrastive learning approach, simultaneously training two encoders to project their outputs into a common, aligned subspace of latent vectors. Figures 4a-c show the geometrical information encoding process. Binary metasurface geometry images (Fig. 4a) enter a geometry encoder (Fig. 4b), which uses a CNN architecture inspired by ResNet [44] to generate a latent vector \mathbf{P}_n for each geometry \mathbf{G}_n , where n is a sample index (Fig. 4c). Each vector \mathbf{P}_n is M -dimensional, where M is a hyperparameter optimized during the training process to reach MOCLIP’s optimal latent space size.

Figures 4d-f depict the spectral information encoding process. This operation begins by concatenating both polarization responses for each metasurface into a single vector \mathbf{S}_n (Fig. 4d). These vectors serve as the input to the spectra encoder (Fig. 4e), which uses an MLP architecture to produce the corresponding latent vectors $\{\mathbf{C}_1, \mathbf{C}_2, \mathbf{C}_3, \dots, \mathbf{C}_N\}$ (Fig. 4f). The Supplementary materials provide additional information on the MOCLIP architecture.

Figure 4g shows the similarity matrix obtained by computing the pairwise dot products between the normalized latent vectors from the two geometry and spectra input modalities. Computing the cross-entropy loss [45] between the similarity matrix and an identity matrix achieves contrastive learning by promoting the alignment of matching pairs while penalizing mismatches. The Methods

section provides additional details on the training process.

Zero-shot prediction

In deep learning, zero-shot prediction assesses a model’s capability to infer classes or inputs not explicitly encountered during training. This step is achieved by leveraging a shared embedding space that preserves semantic relationships. For example, a CLIP model trained solely on photographs of objects can accurately classify stylized drawings of the same objects [40, 46]. This capability is a defining feature of FMs, enabling the reduction of annotation costs and turnaround times, continued functionality in "open-world" settings where new concepts can appear, and model usage for long-tail use cases with scarce examples [47]. MOCLIP delivers zero-shot nanophotonic inverse design capabilities, enabling fast identification of many metasurface geometries that can furnish a previously unseen target spectral response.

Figure 5a-c illustrates MOCLIP’s zero-shot prediction process. The process starts by encoding the target spectrum S_t with the spectra encoder to produce its latent-space representation C_t (Fig. 5a). Next, MOCLIP generates a set of probe geometries G_n (Fig. 5b) and encodes each through the geometry encoder to obtain their corresponding latent-space representations P_n . By computing the cosine similarity between the spectrum’s latent vector and each of the probe geometry’s latent vectors, MOCLIP generates a score vector indicating how closely each probe geometry matches the target spectrum (Fig. 5c). MOCLIP then selects the best-rated geometry (Fig. 5c, yellow cell) as its prediction.

We evaluate MOCLIP’s zero-shot performance by calculating the Top- k retrieval accuracy, a primary metric for assessing an FM [48]. This metric quantifies the proportion of queries in which a model retrieves the correct match within the first k candidates of a ranked retrieval list. Figure 5d reports MOCLIP’s Top- k retrieval accuracy for k ranging from 1 to 20 evaluated on a test set comprising 46 653 unseen samples (see Methods). For each target spectrum in the test set, the model retrieves the top k most similar geometries from the same set, based on the cosine similarity of the latent space vectors. The accuracy is the proportion of cases where the correct geometry appears among the Top- k retrieved candidates. MOCLIP achieves a Top-1 retrieval accuracy of nearly 75%, surpasses 95% at Top-5, and exceeds 98% at Top-10. In a comparable text-to-image retrieval task, the original CLIP model achieves Top-1, Top-5, and Top-10 accuracies of 68.7%, 90.6%, and 95.2% on the Flickr30k dataset, and 37.8%, 62.4%, and 72.2% on the MS-COCO 5k test set, respectively [40]. A similar evaluation in the materials science domain (predicting crystalline structure from the density of states) reports Top-1, Top-5, and Top-10 retrieval accuracies of approximately 40%, 75%, and 85%, respectively [49].

MOCLIP’s zero-shot prediction offers high generative throughput over conventional inverse design models. The process begins by generating a database of candidate geometries using the same algorithm as during dataset creation. MOCLIP then encodes each candidate geometry into a latent-space representation using the geometry encoder (Fig. 5b). These operations yield a probe database comprising metasurface geometries and their latent vectors, with a throughput exceeding 7000 designs per second. This approach provides a distinctive advantage in that the probe geometries can be customized and filtered during the initial database generation stage. This feature allows

seamless incorporation of fabrication tolerances or application-specific constraints directly from database creation, while requiring no modifications to the model architecture or retraining.

Once generated, the database supports inverse design inference at a rate exceeding 10^9 probe geometries per second for a specified accuracy. Comparing the experimentally measured spectra of MOCLIP’s predicted geometries against the target spectra provides the model’s zero-shot prediction accuracy as a function of the probe database size. Figure 5e shows the statistical distribution of the MSE between 10 000 randomly sampled target spectra and the spectra of MOCLIP’s predicted geometries plotted against the number of probe geometries in the database. The shaded regions indicate quantile bands: below the 25th percentile (green), between the 25th and 75th percentiles (blue), and between the 75th and 95th percentiles (red). When the probe database size exceeds 10^4 samples, 95% of the target samples achieve an $\text{MSE} < 10^{-2}$, establishing a 10% transmission deviation as an upper bound for the reliable inverse design [42]. At a database size of 10^4 samples and an accuracy level of $\text{MSE} = 10^{-2}$, MOCLIP achieves inverse design throughput of one high-fidelity solution, every $5 \mu\text{s}$. This performance represents a $10^2\times$ speedup over convolutional generative adversarial network (cGAN) models [35] and a $10^6\times$ improvement over state-of-the-art diffusion-based inverse design models [50], while providing superior accuracy. As an example use case, MOCLIP can complete the inverse design of an entire 4-inch wafer filled with $5 \mu\text{m}$ square metasurfaces in 20 minutes, a task typically requiring weeks or months at this resolution using state-of-the-art approaches.

MOCLIP’s symmetric treatment of metasurface geometries and their spectra enables zero-shot prediction of spectral responses from target geometries, effectively framing spectra prediction as

a cross-modal retrieval task. By leveraging a database of measured spectral responses, MOCLIP replaces time-consuming electrodynamic simulations with fast, zero-shot predictions, achieving speedups of up to 10^7 , while incorporating experimentally validated data. This approach achieves accuracy comparable to that of the inverse design scenario. The Supplementary Materials provide a pipeline for MOCLIP’s zero-shot prediction of spectral responses from target geometries and metrics for this task.

Design by latent space optimization

Beyond zero-shot prediction, MOCLIP’s shared latent space enables an alternative inverse design strategy that optimizes latent space vectors. This approach replaces time-intensive electrodynamic simulations of probe geometries [1, 2] with rapid inference through the geometry encoder. It substitutes the traditional spectrum-matching loss with a similarity-based loss computed between the latent vectors of the target spectrum and candidate geometries. While zero-shot prediction prioritizes high-throughput design generation, latent space optimization emphasizes high-fidelity solutions.

Figure 6a-e illustrates the optimization pipeline. The procedure begins by passing the target spectrum \mathbf{S}_t through the spectra encoder, resulting in its corresponding latent vector \mathbf{C}_t (Fig. 5a). Simultaneously, the geometry encoder processes a probe geometry \mathbf{G}_n to produce its latent vector \mathbf{P}_n (Fig.5b). The same geometry generator used during dataset creation produces these probe geometry candidates (Fig. 5c). The optimization routine maximizes the similarity score $\mathbf{C}_t \cdot \mathbf{P}_n$

by applying particle swarm optimization (PSO) [51] (Fig.6d) to search the generator’s parameter space for the optimal geometry. This optimization continues until the algorithm finds a probe geometry whose latent representation closely matches that of the target spectrum, resulting in an optimized geometry \mathbf{G}_f (Fig.6e).

Figure 6f presents the performance of latent space optimization-based inverse design, evaluated on 1000 target spectra. The plot shows the statistical distribution of the MSE between the target spectra and the experimentally measured spectra of the predicted geometries as a function of the number of PSO iterations. The shaded regions indicate quantile bands in the same way as in the zero-shot prediction case. The process begins with 100 randomly generated probe geometries, whose zero-shot predictions yield relatively high MSE values. As the optimization iteratively adjusts the probe geometries to maximize the similarity score, the 95th percentile MSE drops below 10^{-2} after 10 iterations and reaches 10^{-3} by iteration 30. These results are competitive with and sometimes exceed those reported for existing state-of-the-art models [35, 37]. Figure 7 provides representative examples of the inverse-designed geometries obtained through latent space optimization and comparisons between their experimentally measured spectra and the corresponding target spectra.

Information Storage

MOCLIP’s ability to encode arbitrary information sequences into a shared geometry-spectra latent space provides a platform for long-term optical information storage. Figure 8a presents an

overview of the concept. The initial step is the inverse design and fabrication of metasurface arrays whose elements have unique representations in the shared geometry-spectra latent space. Then, reading the metasurface’s transmission spectra with a hyperspectral transmission microscope and passing this information to MOCLIP’s spectra encoder generates the spectra latent vector \mathbf{S} . Feeding this latent vector to a quantizer furnishes the data stored in the metasurface. Figure 8b presents the distribution of variable values in the first six latent vector dimensions. The Kolmogorov–Smirnov test (K-S test) [52] compares their distribution to a continuous Gaussian probability density function to better characterize and quantify the latent vectors. A resulting K-S score of 0.014 indicates that the latent vector is a 64-dimensional, Gaussian-distributed signal. This finding guides choosing a high-dimensional vector quantization (VQ) strategy, commonly adapted in modern LLM training [53]. The VQ maps the latent vector to a discrete set of candidate vectors, namely codebook centroids, and iterates them to minimize the distortion error during the mapping. Figure 8c exemplifies the VQ strategy applied at the first two dimensions S_1, S_2 of the latent space, where K -means clustering constructs the mapping and locates the codebook centroids. This example applies a bit depth of 2 to each dimension, resulting in a codebook size of $K = 16$. Rate-distortion theory [54] allows an exploration of the theoretical limit of MOCLIP’s storage capacity. Equation 2 calculates the latent space’s rate-distortion bound \mathbf{R} , representing the maximum quantization bit depth applicable.

$$\mathbf{R} = \left\lceil \sum_i \frac{1}{2} \log_2 \left(\frac{\sigma_i^2}{D_i} \right) \right\rceil, \quad 0 < D_i < \sigma_i^2 \quad (2)$$

Here, σ_i represents the variance of the latent dimension i and D_i describes the distortion, defined as the MSE between the latent vectors generated from the spectral dataset and their duplicates. Cal-

culating D_i and σ_i on the metasurface spectra dataset results in a rate-distortion bound of $\mathbf{R} = 126$. This value indicates that it’s possible to encode a maximum of 126 bits of information into the 64-dimensional latent space of each metasurface. Figure 8d plots the information density of the proposed technology against the lateral unit size of square metasurfaces. In the current experimental realization, each metasurface has a $6\ \mu\text{m}$ unit size, corresponding to an information density of $3.34\ \text{Mbit}/\text{mm}^2$, nearly doubling that of DVD (Fig. 8d, red dashed line). However, reducing the metasurface sizes can yield orders of magnitude improvement of the information density. Fig. 8d shows that MOCLIP’s information storage density surpasses that of Blu-ray (yellow dashed line) when the metasurface has a unit size below $3.5\ \mu\text{m}$. The theoretical upper bound of information density with the current setup results from repeating the preceding analysis for metasurface unit sizes down to the Rayleigh criterion diffraction limit, corresponding to $1.056\ \mu\text{m}$, and yields $107.85\ \text{Mbit}/\text{mm}^2$.

Discussion

This work develops and implements MOCLIP, an FM framework for inverse design that learns a shared latent space to embed metasurface geometries and their corresponding spectra jointly. The FM training pipeline leverages an experimentally generated dataset comprising 466 537 silicon-on-glass metasurface geometry-spectra pairs spanning 42 design degrees of freedom. MOCLIP dataset enhances over ninefold the size and increases to nearly threefold the design complexity of the largest previously reported metasurface–spectra dataset, incorporating typical missing in-

formation from simulations, such as, e.g., fabrication tolerances and measurement uncertainties. MOCLIP experimental workflow generates an entire FM dataset at a rate of around 35 structures per minute, making this approach over thirty times faster than strategies based on computational electrodynamic approaches run on supercomputers. Adopting state-of-the-art manufacturing techniques, such as immersion lithography [55], can further increase this rate, enabling orders of magnitude improvements in generating robust and physically accurate datasets for nanophotonic FMs. We demonstrate multiple applications of MOCLIP for inverse design, including zero-shot prediction and generative latent space optimization. These capabilities surpass traditional reconstruction-based deep learning approaches in nanophotonics, offering up to six orders of magnitude faster inference and a tenfold improvement in accuracy [35, 50] while retaining high flexibility to incorporate fabrication-related design constraints. MOCLIP’s zero-shot prediction achieves inverse design at a speed of approximately $2 \cdot 10^5$ target spectra per second while maintaining an MSE below 10^{-2} , making wafer-scale, high-throughput inverse design feasible. At the same time, when higher accuracy is required, MOCLIP’s latent space optimization enables inverse design with an order-of-magnitude improvement, reducing the MSE below 10^{-3} within 30 PSO iterations.

We concluded this work by demonstrating an application of MOCLIP for optical information storage. Our approach leverages the shared geometry-spectra latent space to encode information. It applies VQ to model the distribution of latent variables and to optimize the quantization strategy. With the current experimental realization, MOCLIP achieves an information density of 3.34 Mbit/mm², comparing favorably to last-generation optical storage devices. This concept can be extended to outperform the state-of-the-art by shrinking the metasurface unit size. The theoretical

upper bound of information density is calculated to be 0.1 Gbit/mm^2 with a metasurface unit size of $1.056 \mu\text{m}$, at the diffraction limit of the current optical system.

Methods

Geometries generation

It uses a Python-based software tool that stochastically populates a square cell with a fixed lattice period with a user-specified number of primitives (rectangles, ellipses, and rings). For each primitive, the algorithm samples the center position and in-plane dimensions (for rings, both outer and inner dimensions), accepting the draw only if the feature lies entirely within the cell. To satisfy fabrication constraints, the algorithm enforces limits on each shape's dimensions, the spacing between features, and the minimum feature size. It requires every shape dimension to be at least 100 nm , and the feature size and inter-feature gap to be no smaller than 50 nm . The software samples each design on a discrete grid with lattice periods of 300 nm , 400 nm , 500 nm and 600 nm and silicon thicknesses of 150 nm , 178 nm and 195 nm . To keep the design space within practical limits, it allows at most four primitives per unit cell, resulting in 42 independent geometric degrees of freedom. Within these bounds, the software generated 546 120 unique metasurface designs.

Fabrication

The process begins with cleaning a fused silica wafer using acetone and isopropyl alcohol, followed by the deposition of a uniform amorphous silicon layer via low-pressure chemical vapor deposition (LPCVD). The thickness of the silicon layer is precisely controlled using ellipsometry (UVISEL Plus, HORIBA). The wafer is then diced into 15 mm wide and 500 μm thick pieces to serve as base samples. A positive electron beam resist, AR-P 6200.04 (Allresist), is spin-coated on the samples at 6000 RPM for 60 s, followed by a bake on a hotplate for 90 s at 150 °C. Subsequently, a conductive polymer, AR-PC 5090.02 (Allresist), is spin-coated at 4000 RPM for 60 s and baked at 100 °C for 1 min. Metasurface patterns are written using a JEOL JBX-6300FS electron beam lithography system at 100 kV. After patterning, the conductive polymer is removed by submerging the sample in deionized water for 60 s. The resist is developed using AR 600-546 (Allresist) for 60 s, followed by O-Xylene for 7 s to sharpen feature edges. A 22 nm chromium layer is deposited via electron beam evaporation to form an etch mask. Unwanted chromium is lifted off by submerging the sample in AR 600-71 (Allresist) for 10 minutes, followed by one minute of sonication. Reactive ion etching with a CHF_3 and SF_6 mixture is used to remove unprotected silicon and expose the underlying substrate. Finally, the chromium mask is removed by submerging the sample in a mixture of perchloric acid and ceric ammonium nitrate (TechniEtch Cr01, MicroChemicals) for 60 s.

Foundation model training

The dataset is divided into three subsets: training (373 230 samples; 80%), validation (46 654 samples; 10%), and test (46 653 samples; 10%). The model is trained exclusively on the training set, using the validation to monitor performance at the end of each epoch and guide model selection. The test set was reserved to evaluate the final model performance after the training.

The model is trained for 140 epochs using a three-stage learning rate schedule: 1×10^{-4} for epochs 1–60, 5×10^{-5} for epochs 61–100, and 3×10^{-5} for epochs 101–140. Adam optimizer [56] updates the model parameters. The network contains approximately 11.8 million trainable parameters. The Supplementary Materials further detail the model architecture. All training and evaluation are conducted on a workstation equipped with an AMD Ryzen Threadripper PRO 5955WX 16-core processor, 128 GB of RAM, and an NVIDIA GeForce RTX 4090 GPU.

References

1. Li, Z. *et al.* Empowering Metasurfaces with Inverse Design: Principles and Applications. *ACS Photonics* **9**, 2178–2192 (2022).
2. Sunae *et al.* Revisiting the Design Strategies for Metasurfaces: Fundamental Physics, Optimization, and Beyond. *Advanced Materials* **35**, 2206399 (2023).

3. Wang, Q. *et al.* The Transformational Dive of Nanophotonics Inverse Design from Deep Learning to Artificial General Intelligence. *APL Photonics* **9** (2024).
4. Seo, J. *et al.* Deep-learning-driven End-to-End Metalens Imaging. *Advanced Photonics* **6**, 066002 (2024).
5. Getman, F. *et al.* Broadband Vectorial Ultrathin Optics with Experimental Efficiency up to 99% in the Visible Region via Universal Approximators. *Light: Science & Applications* **10**, 47 (2021).
6. Wang, Q. *et al.* Advancing Statistical Learning and Artificial Intelligence in Nanophotonics Inverse Design. *Nanophotonics* **11**, 2483–2505 (2022).
7. Deng, R. *et al.* Inverse Design in Photonic Crystals. *Nanophotonics* **13**, 1219–1237 (2024).
8. He, J. *et al.* Plasmonic Nanoparticle Simulations and Inverse Design Using Machine Learning. *Nanoscale* **11**, 17444–17459 (2019).
9. MacLellan, B. *et al.* Inverse Design of Photonic Systems. *Laser & Photonics Reviews* **18**, 2300500 (2024).
10. Makarenko, M. *et al.* Hardware-Accelerated Integrated Optoelectronic Platform towards Real-Time High-Resolution Hyperspectral Video Understanding. *Nature Communications* **15**, 7051 (2024).
11. Wang, Z. *et al.* Computational Optical Imaging: On the Convergence of Physical and Digital Layers. *Optica* **12**, 113–130 (2025).

12. Al-Ashwal, N. H. *et al.* Deep Learning for Optical Sensor Applications: A Review. *Sensors* **23**, 6486 (2023).
13. Ma, T. *et al.* OptoGPT: A Foundation Model for Inverse Design in Optical Multilayer Thin Film Structures. *Opto-Electronic Advances* **7** (2024).
14. Liang, Y. *et al.* Foundation Models for Time Series Analysis: A Tutorial and Survey in *Proceedings of the 30th ACM SIGKDD Conference on Knowledge Discovery and Data Mining* (2024).
15. Zhou, C., Li, Q., Li, C., *et al.* A Comprehensive Survey on Pretrained Foundation Models: A History from BERT to ChatGPT. *International Journal of Machine Learning & Cybernetics* (2024).
16. Fei, N. *et al.* Towards Artificial General Intelligence via a Multimodal Foundation Model. *Nature Communications* **13**, 3094 (2022).
17. Awais, M. *et al.* Foundation Models Defining a New Era in Vision: a Survey and Outlook. *IEEE Transactions on Pattern Analysis and Machine Intelligence* (2025).
18. Moor, M. *et al.* Foundation models for generalist medical artificial intelligence. *Nature* **616**, 259–265 (2023).
19. Zhou, Y. *et al.* A Foundation Model for Generalizable Disease Detection from Retinal Images. *Nature* **622**, 156–163 (2023).
20. Wang, X. *et al.* A Pathology Foundation Model for Cancer Diagnosis and Prognosis Prediction. *Nature* **634**, 970–978 (2024).

21. Nguyen, T. *et al.* ClimaX: A Foundation Model for Weather and Climate. *arXiv preprint arXiv:2301.10343* (2023).
22. Ahmad, W. *et al.* Chemberta-2: Towards Chemical Foundation Models. *arXiv preprint arXiv:2209.01712* (2022).
23. Batatia, I. *et al.* A Foundation Model for Atomistic Materials Chemistry. *arXiv preprint arXiv:2401.00096* (2023).
24. Firoozi, R. *et al.* Foundation models in robotics: Applications, challenges, and the future. *The International Journal of Robotics Research*, 02783649241281508 (2023).
25. Kang, C. *et al.* Large-scale Photonic Inverse Design: Computational Challenges and Breakthroughs. *Nanophotonics* **0** (2024).
26. Huang, W. R., Emam, Z., Goldblum, M., Fowl, L., Terry, J., Huang, F. & Goldstein, T. *Understanding Generalization through Visualizations in Proceedings of the 37th International Conference on Machine Learning (ICML)* (2020), 87–97.
27. Pope, P., Zhu, S., Abdelkader, A., Goldblum, M. & Goldstein, T. The intrinsic dimension of images and its impact on learning. *arXiv preprint arXiv:2104.08894* (2021).
28. Gong, S., Boddeti, V. N. & Jain, A. K. *On the intrinsic dimensionality of image representations in Proceedings of the IEEE/CVF Conference on Computer Vision and Pattern Recognition (CVPR)* (2019), 4716–4724.
29. Camastra, F. & Staiano, A. Intrinsic dimension estimation: Advances and open problems. *Information Sciences* **328**, 26–41 (2016).

30. Sharma, U. & Kaplan, J. Scaling laws from the data manifold dimension. *Journal of Machine Learning Research* **23**, 1–34 (2022).
31. Hestness, J., Narang, S., Ardalani, N., Diamos, G., Jun, H., Kianinejad, H., Patwary, M., Yang, Y. & Zhou, Y. Deep learning scaling is predictable, empirically. *arXiv preprint arXiv:1712.00409* (2017).
32. Cherti, M., Kirillov, A., Beyer, L., Zhai, X., Houlsby, N., Kolesnikov, A. & Djolonga, J. *Reproducible scaling laws for contrastive language-image learning* in *Proceedings of the IEEE/CVF Conference on Computer Vision and Pattern Recognition* (2023), 3607–3617.
33. Grbcic, L., Park, M., Elzouka, M., Prasher, R., Müller, J., Grigoropoulos, C. P., Lubner, S. D., Zorba, V. & de Jong, W. A. Inverse design of photonic surfaces via multi fidelity ensemble framework and femtosecond laser processing. *npj Computational Materials* **10**, 1–10 (2024).
34. Yao, T., Huang, T., Yan, B., Ge, M., Yin, J., Peng, C., Li, L., Sun, W. & Shum, P. P. Inverse design of dispersion for photonic devices based on LSTM and gradient-free optimization algorithms hybridization. *Journal of the Optical Society of America B* **40**, 1525–1532 (2023).
35. Liu, Z., Zhu, D., Rodrigues, S. P., Lee, K.-T. & Cai, W. Generative Model for the Inverse Design of Metasurfaces. *Nano Letters* **18**, 6570–6576 (2018).
36. Roberts, N. B. & Hedayati, M. K. A deep learning approach to the forward prediction and inverse design of plasmonic metasurface structural color. *Applied Physics Letters* **119**, 061101 (2021).
37. Wang, Y., Yang, Y., Wang, Z., Zheng, Y., Luo, X. & Qiu, M. End-to-end diverse metasurface design and evaluation using an invertible neural network. *Nanomaterials* **13**, 2561 (2023).

38. Malkiel, I., Mrejen, M., Nagler, A., Arieli, U., Wolf, L. & Suchowski, H. Plasmonic nanostructure design and characterization via deep learning. *Light: Science & Applications* **7**, 60 (2018).
39. Clini de Souza, A., Lanteri, S., Hernández-Figueroa, H. E., Abbarchi, M., Grosso, D., Kerzabi, B. & Elsaywy, M. Back-propagation optimization and multi-valued artificial neural networks for highly vivid structural color filter metasurfaces. *Scientific Reports* **13** (2023).
40. Radford, A. *et al.* *Learning Transferable Visual Models from Natural Language Supervision* in *Proceedings of the 38th International Conference on Machine Learning* (PMLR, 2021).
41. Rombach, R., Blattmann, A., Lorenz, D., Esser, P. & Ommer, B. High-Resolution Image Synthesis with Latent Diffusion Models. *Proceedings of the IEEE/CVF Conference on Computer Vision and Pattern Recognition*, 10684–10695 (2022).
42. Chen, M. K., Zhu, L., Yang, C., Qiu, C.-W. & Tsai, D. P. Artificial intelligence in meta-optics. *Chemical Reviews* **122**, 15356–15413 (2022).
43. Blu-ray Disc Association. *White Paper Blu-ray Disc™ Format 1.C Physical Format Specifications for BD-ROM*. Oct. 2010.
44. He, K., Zhang, X., Ren, S. & Sun, J. Deep Residual Learning for Image Recognition. *arXiv preprint arXiv:1512.03385v1* (2015).
45. Bishop, C. M. *Pattern Recognition and Machine Learning* Softcover reprint of the original 1st edition 2006 (corrected at 8th printing 2009). 738 pp. (Springer New York, New York, NY, 2016).

46. Girdhar, R., Gkioxari, G., Carreira, J., Singh, M., Wu, Z. & Feichtenhofer, C. *ImageBind: One Embedding Space To Bind Them All* in *Proceedings of the IEEE/CVF International Conference on Computer Vision (ICCV)* (2023).
47. Liu, F., Chen, D., Guan, Z., Zhou, X., Zhu, J., Ye, Q., Fu, L. & Zhou, J. RemoteCLIP: A Vision Language Foundation Model for Remote Sensing. *IEEE Transactions on Geoscience and Remote Sensing*. arXiv:2306.11029 (2023).
48. Petersen, F., Kühne, H., Borgelt, C. & Deussen, O. *Differentiable Top-k Classification Learning* in *Proceedings of the 39th International Conference on Machine Learning (ICML)* **162** (2022), 17656–17668.
49. Moro, V. *et al.* Multimodal Learning for Crystalline Materials. *arXiv preprint arXiv:2312.00111* (2023).
50. Zhu, L., Hua, W., Lv, C. & Liu, Y. Rapid Inverse Design of High Degree of Freedom Meta-Atoms Based on the Image-Parameter Diffusion Model. *Journal of Lightwave Technology* **42**, 5269–5278 (2024).
51. Makarenko, M., Burguete-Lopez, A., Getman, F. & Fratolocchi, A. Robust and scalable flat-optics on flexible substrates via evolutionary neural networks. [Currently under a second round of review in *Advanced Intelligent Systems*] (2021).
52. Simard, R. & L'Ecuyer, P. Computing the Two-Sided Kolmogorov-Smirnov Distribution. *Journal of Statistical Software* **39** (2011).

53. Liu, Y., Wen, J., Wang, Y., Ye, S., Zhang, L. L., Cao, T., Li, C. & Yang, M. *VPTQ: Extreme Low-bit Vector Post-Training Quantization for Large Language Models* arXiv: 2409.17066 [cs]. <http://arxiv.org/abs/2409.17066> (2025). Pre-published.
54. Cover, T. M. & Thomas, J. A. *Elements of Information Theory* Second edition. 1 p. (Wiley-Interscience, Hoboken, N.J, 2006).
55. Li, N., Xu, Z., Dong, Y., Hu, T., Zhong, Q., Fu, Y. H., Zhu, S. & Singh, N. Large-Area Metasurface on CMOS-compatible Fabrication Platform: Driving Flat Optics from Lab to Fab. *Nanophotonics* **9**, 3071–3087 (Sept. 2, 2020).
56. Kingma, D. P. & Ba, J. Adam: A method for stochastic optimization. *arXiv preprint arXiv:1412.6980* (2014).

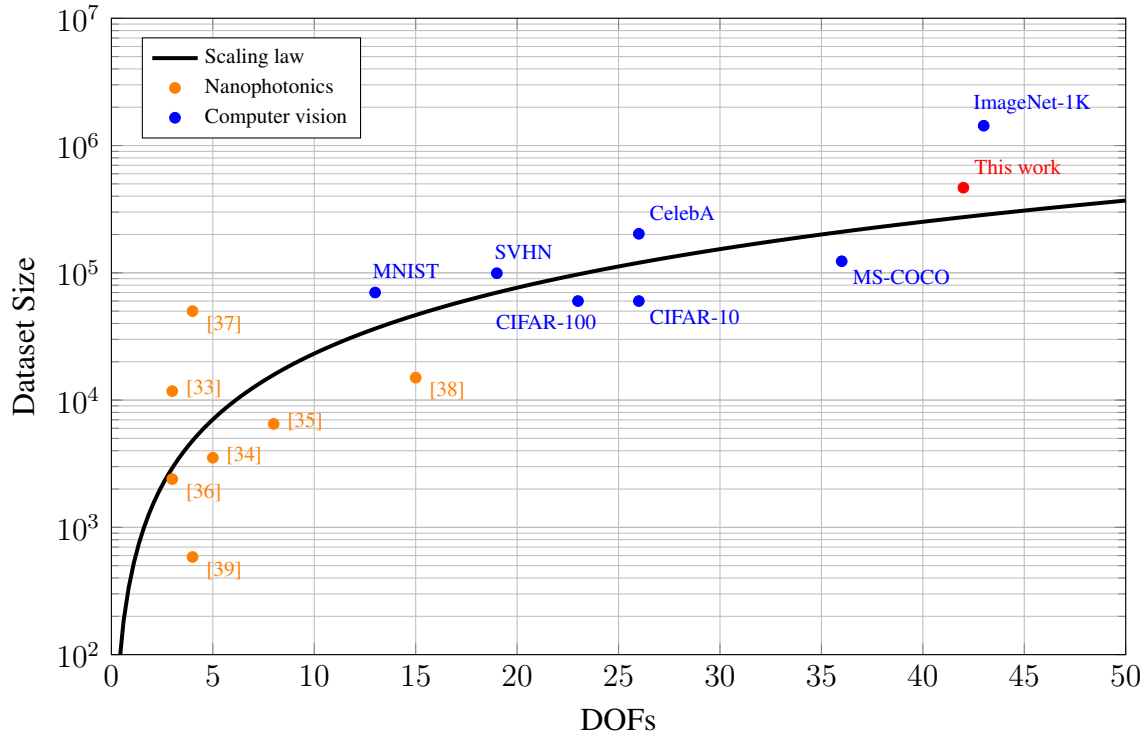


Figure 1: **State-of-the-art nanophotonic and computer vision datasets.** Dataset size vs DOFs, illustrating empirical scaling trends. Computer vision dataset sizes and DOFs taken from [27]. The scaling law is driven by the equation $N = kd^\alpha$, with fitted parameters $\alpha = 1.72$ and $k = 442$.

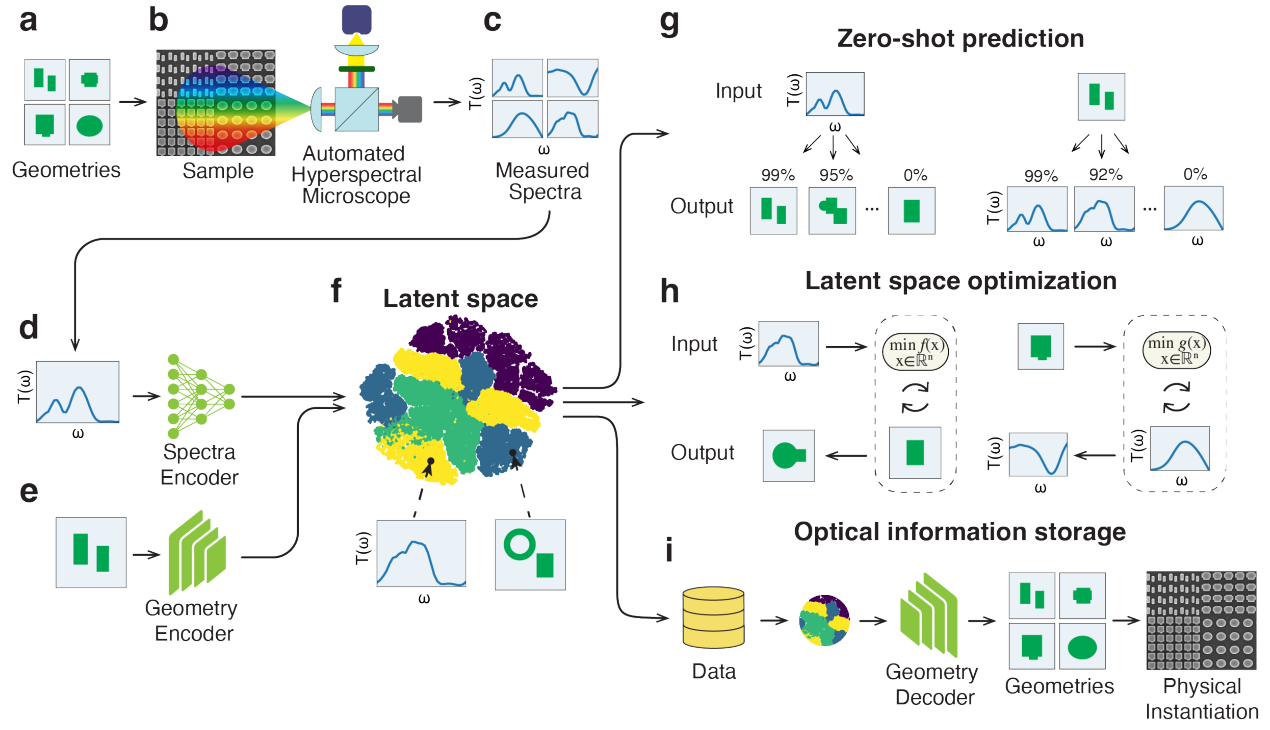


Figure 2: **MOCLIP concept.** **a.** Dataset of randomly generated free-form metasurface geometries. **b.** Experimental realization and characterization of the designs using an automated hyperspectral microscope. **c.** Dataset of measured spectra corresponding to the free-form metasurface designs. **d.** Encoding of experimental metasurface spectral responses. **e.** Encoding of metasurface geometries. **f.** Shared latent space for spectral and geometrical information. **g.** Zero-shot prediction for inverse design (left) and spectra prediction (right). **h.** Latent space optimization for inverse design (left) and spectra prediction (right). **i.** Optical information storage via physical implementation of latent space information.

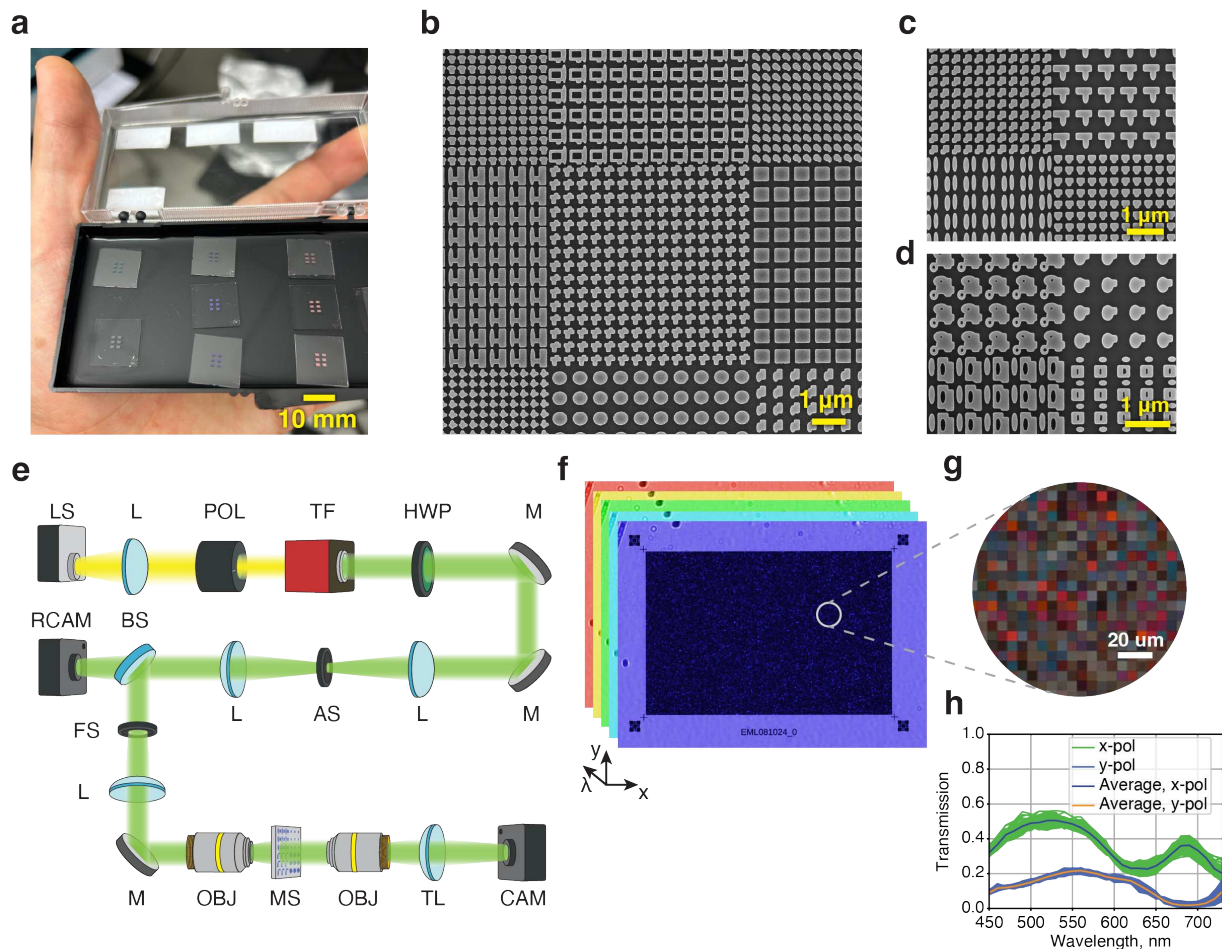


Figure 3: **Dataset generation.** **a.** A set of fabricated samples, each carrying six metasurface arrays of amorphous silicon on a fused-silica substrate, totaling 136 530 dataset samples per substrate. **b-d.** SEM pictures of the fabricated metasurface arrays. **e.** Hyperspectral transmission microscopy setup. **f.** Spatial and spectral data hypercube of a metasurface array under fixed polarization conditions, shown in false colors for visualization. **g.** Expanded view of the metasurface array under broadband illumination. **h.** Example spectra extracted from the pixels of a single metasurface pad for x- and y-polarized illumination (green and blue sets of curves) and average pixel responses (black and orange curves).

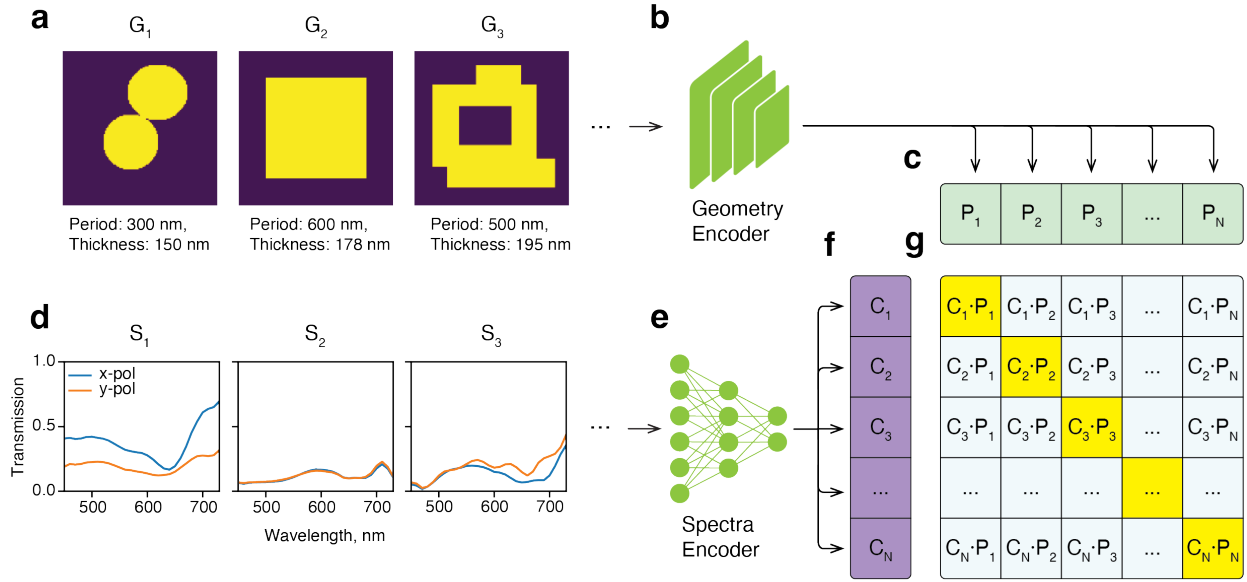


Figure 4: **MOCLIP training**. **a**. Representation of geometrical metasurface information as 128×128 binary images with period and thickness parameters. **b**. Geometry encoder, comprising a CNN architecture. **c**. 64-dimensional latent vectors produced by the geometry encoder. **d**. Spectral information represented by two 29-dimensional vectors for x- and y-polarizations. **e**. Spectra encoder based on an MLP architecture. **f**. 64-dimensional latent vectors produced by the spectra encoder. **g**. Similarity matrix containing pairwise dot products between latent vectors from both modalities. Yellow entries correspond to matching geometry–spectra pairs trained to have similarity values close to 1, with the rest indicating non-matching pairs trained to approach zero.

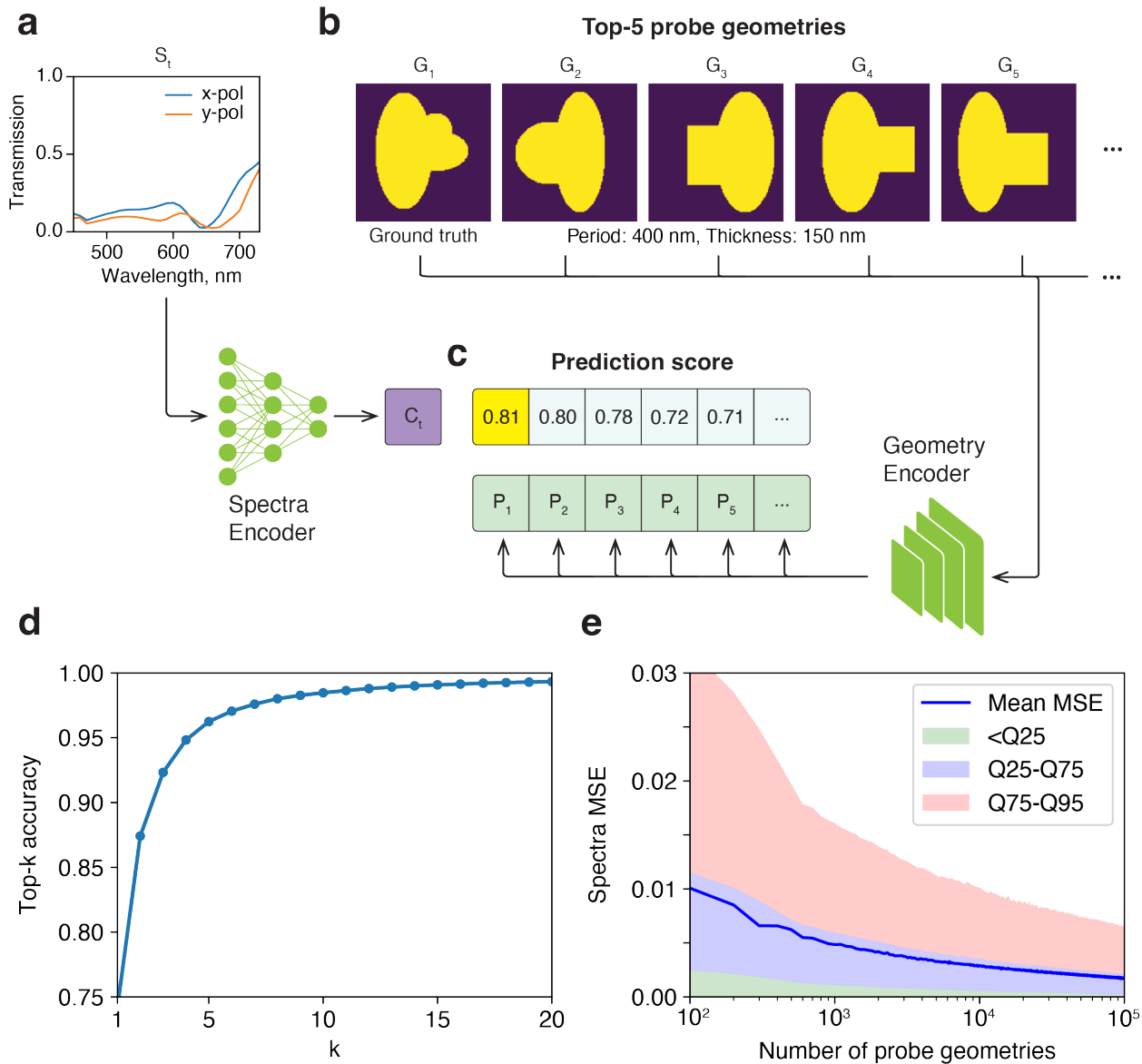


Figure 5: **Zero-shot prediction.** **a.** Target spectrum encoding into a latent vector. **b.** Encoding of probe geometries, including the ground truth one, into latent vectors. **c.** Similarity score vector between the target spectrum and the candidate geometry latent vectors. The yellow cell indicates the best matching score for the predicted geometry. **d.** Top-k accuracy for the test dataset. **e.** Statistical distribution of the MSE between the target spectrum and measured spectra of the predicted geometries as a function of the number of probe geometries. Shaded bands indicate quantile regions; the solid line indicates the mean.

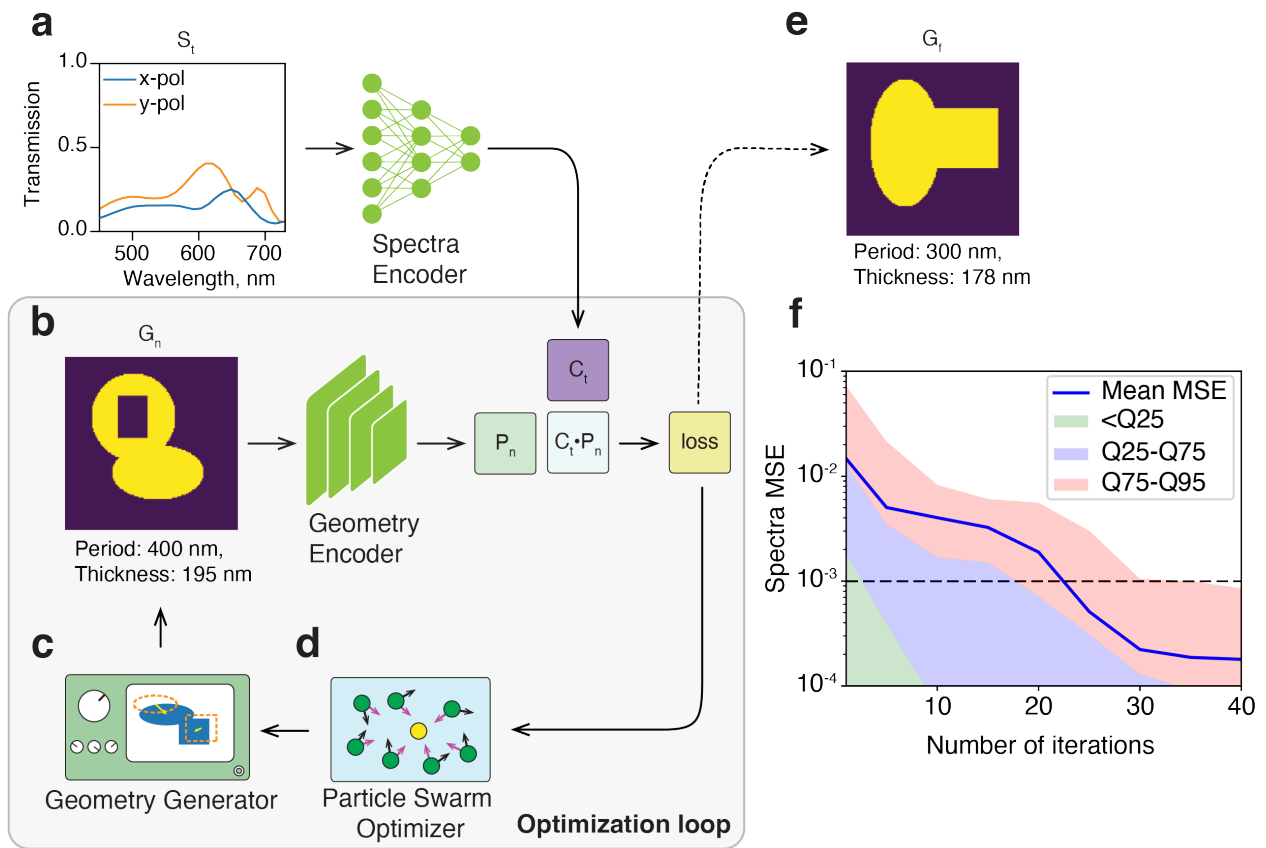


Figure 6: **Latent space optimization.** **a.** Target spectrum encoding into a latent-space vector. **b.** Intermediate geometry prediction encoding into a latent-space vector. **c.** Geometry generator with trainable parameters. **d.** Optimizer for the geometry generator. **e.** Optimized geometry prediction. **f.** Statistical distribution of the MSE between the target spectrum and measured spectra of the predicted geometries as a function of the number of the Optimizer's iterations. Shaded bands indicate quantile regions, the solid line indicates the mean, and the dashed line indicates the MSE = 10^{-3} level.

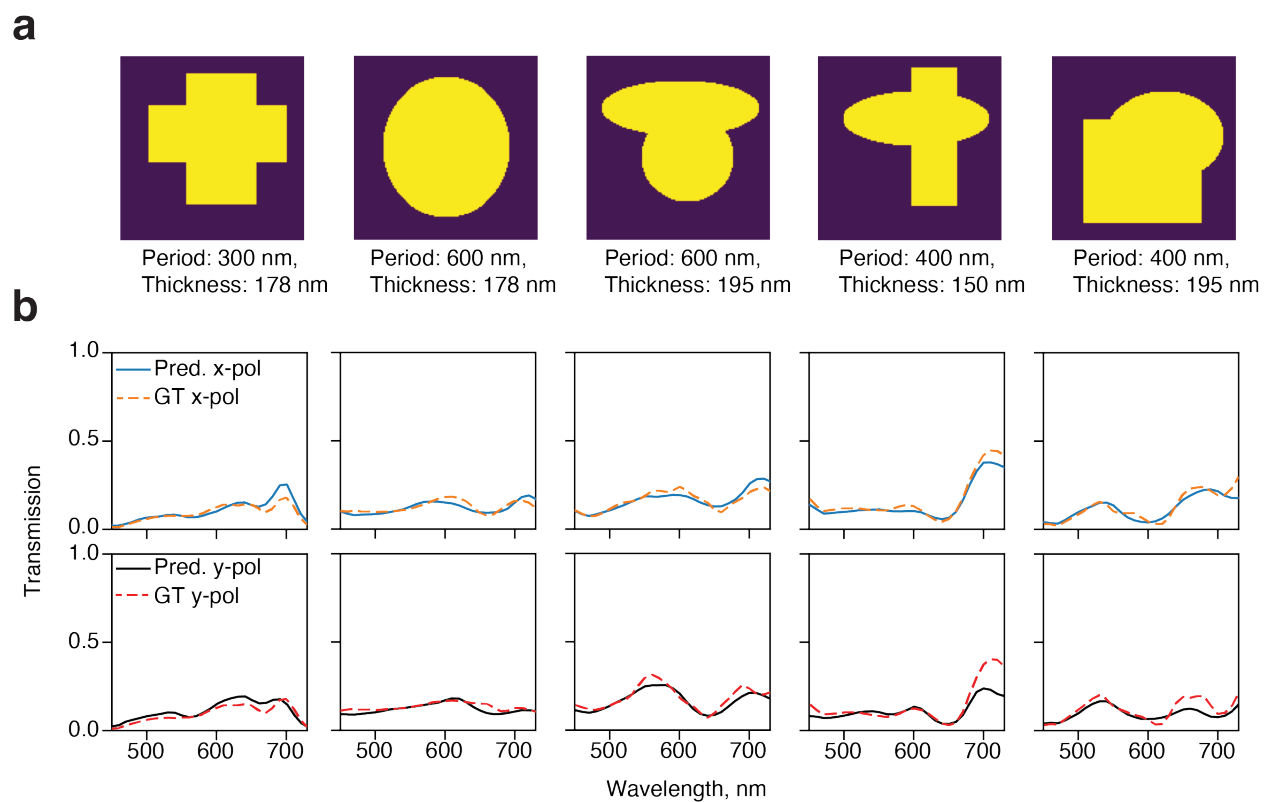


Figure 7: **Latent space optimization results.** **a.** Examples of geometries predicted by the latent space optimization. **b.** Comparison between the target spectra (GT, dashed lines) and experimentally measured spectra (Pred., solid lines) for the predicted geometries

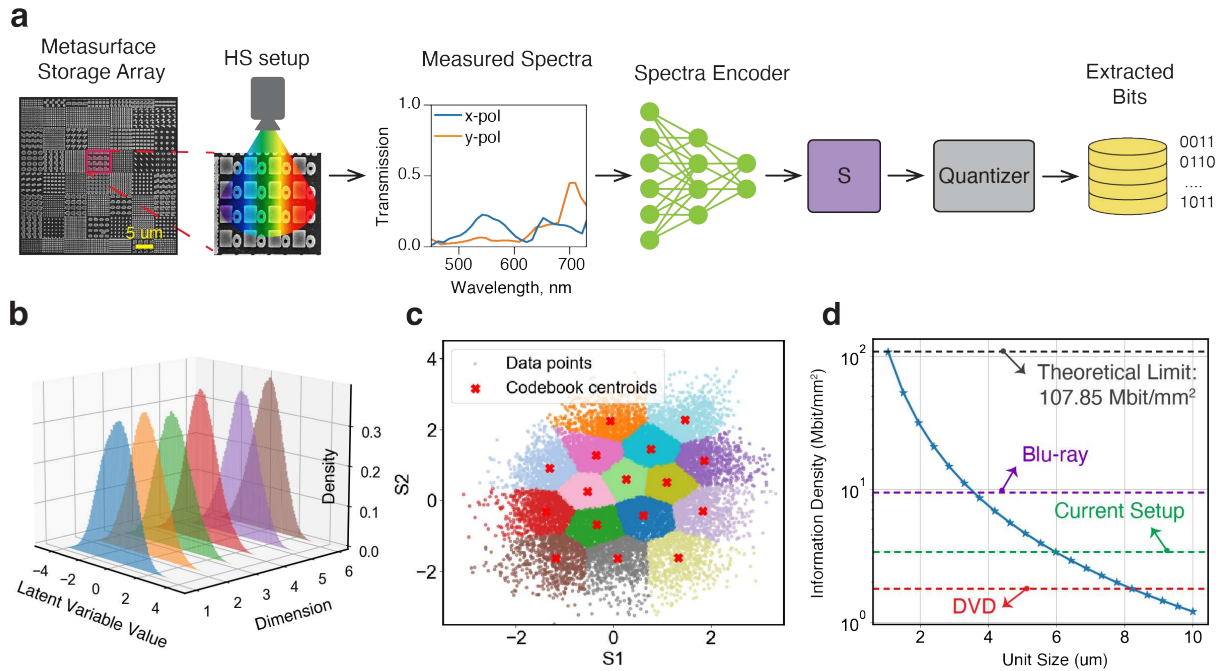


Figure 8: **Optical storage based on latent space encoding.** **a.** General schematic of optical storage utilizing a metasurface structure's latent space information. **b.** Visualization of the distribution of latent vectors in their first 6 dimensions. **c.** Vector quantization of the latent variables at the first 2 dimensions. **d.** Performance analysis on information density compared to DVD and Blu-ray disks. As the unit size of metasurface decreases, the theoretical density of MOCLIP optical storage outperforms Blu-ray.

Supplementary Materials - MOCLIP: A Foundation Model for Large-Scale Nanophotonics Inverse Design

Sergei Rodionov^{1†}, A. Burguete-Lopez^{1†}, M. Makarenko^{1†}, Q. Wang¹, F. Getman¹, & A. Fratalocchi^{1*}

¹PRIMALIGHT, Faculty of Electrical Engineering; Applied Mathematics and Computational Science, King Abdullah University of Science and Technology, Thuwal 23955-6900, Saudi Arabia

[†] First author with equal contribution.

* Corresponding author. Email: andrea.fratalocchi@kaust.edu.sa.

Experimental setup components

We collimate broadband light from a xenon lamp (HPX-2000, Ocean Optics) with a $10\times$ objective (RMS10X, Thorlabs) and linearly polarize it using a Glan–Taylor prism (DGL10, Thorlabs) before passing it through a liquid crystal tunable bandpass filter (K2VB1, Thorlabs). We drive the filter at its minimum bandwidth (10 nm FWHM at 550 nm) and step it from 450 nm to 730 nm in 10 nm increments. We use a half-wave plate (AHWP10M-600, Thorlabs) to set the required x- or y-polarisation. We then expand the beam two-fold with a 4-f telescope (lenses LA1131-AB and LA1433-AB, Thorlabs) and spatially clean it with an adjustable aperture. We divide the beam with a non-polarising beamsplitter (BSW26R, Thorlabs). One arm images onto a reference CMOS camera (LP126MU, Thorlabs) to monitor the source intensity, and the other continues to the sample arm of the microscope. We trim the beam diameter with a field-stop aperture and then focus it using

a plano-convex lens (LA1509-AB, Thorlabs) onto the back focal plane of a $10\times$ long-working-distance objective (MY10X-823, Thorlabs), establishing Köhler illumination on the sample. A second $10\times$ long-working-distance objective collects the transmitted light and relays it through a 200 mm tube lens (TTL200-S8, Thorlabs) onto the imaging CMOS camera (CS126MU, Thorlabs), yielding high-contrast metasurface images for every wavelength–polarization setting.

We mount the sample on a motorized pitch–yaw platform (PY004Z9, Thorlabs) stacked on a three-axis linear stage (PT3Z9, Thorlabs), providing five motorized degrees of freedom (X , Y , Z , θ_x , θ_y) for precise positioning. A precision rotation mount (CRM1PT, Thorlabs) adds manual rotation about the optical axis, allowing the camera sensor to register the metasurface array angularly. The stage’s travel range is large enough to completely translate the sample from the objective’s field of view, enabling fully automated measurement cycles.

Measurement error analysis.

First, we analyze the optimal number of pixels to average for each metasurface, balancing the trade-off between camera noise and boundary effects. From the noise reduction perspective, averaging over a larger number of pixels minimizes random fluctuations and improves signal stability. However, including pixels near the edges of each metasurface can introduce errors due to optical cross-talk or fabrication imperfections from neighboring structures. To identify the optimal averaging area, we conduct an error analysis by comparing spectra from original structures and their

exact replicas—fabricated and measured independently—while varying the number of averaged pixels. We find that averaging over the central 64 pixels out of 289 provides the best trade-off, yielding the lowest mean spectral deviation of 0.021 (Fig. S1a).

Next, we perform cross-validation on the spectral dataset by comparing each spectrum with that of its corresponding replica, following the same procedure used in the pixel-averaging analysis. Figure S1b shows the results, quantified using root mean squared error (RMSE). To mitigate the influence of fabrication defects, surface contamination, and measurement inconsistencies, we apply a quality control threshold that excludes samples with a mean squared error (MSE) greater than 1×10^{-3} from the dataset. This filtering step retains approximately 85% of the dataset.

Finally, we quantify the measurement uncertainty associated with the validated spectra. Each spectrum carries three independent $1\text{-}\sigma$ uncertainties: (i) camera shot and read noise after five-frame and 8×8 patch averaging, (ii) pixel-to-pixel fabrication variability inside the 8×8 analysis patch, (iii) the wavelength setting accuracy of the liquid-crystal tunable filter (LCTF).

For every structure j and wavelength slice i we first propagate the per-pixel noise $\sigma_{T,m}$. The random error of the pixel average is

$$\sigma_{\text{rand}}(i, j) = \frac{\sqrt{\sum_{m=1}^{N_p} \sigma_{T,m}^2}}{N_p}, \quad (1)$$

where $N_p = 64$. The fabrication spread is

$$\sigma_{\text{fab}}(i, j) = \sqrt{\frac{1}{N_p - 1} \sum_{m=1}^{N_p} [T_m(i, j) - \bar{T}(i, j)]^2}, \quad (2)$$

with \bar{T} being the mean of the 8×8 patch. Fig. S1c shows the wavelength-dependent variation of both error components, with σ_{rand} and σ_{fab} averaged over all structures and plotted as functions of wavelength. The random and fabrication uncertainties combine in quadrature as

$$\sigma_{\text{tot}}(i, j) = \sqrt{\sigma_{\text{rand}}^2 + \sigma_{\text{fab}}^2}, \quad (3)$$

yielding structure and wavelength-averaged values of $\sigma_{\text{rand}} = 0.016$, $\sigma_{\text{fab}} = 0.013$, and $\sigma_{\text{tot}} = 0.026$. In addition, the liquid-crystal tunable filter (LCTF) introduces a separate systematic wavelength uncertainty of ± 0.5 nm, specified by the manufacturer.

MOCLIP architecture

Figure S2 illustrates the architecture of MOCLIP's geometry and spectra encoders. In the geometry encoder (Fig. S2a), the input geometry \mathbf{G} is represented as a 128×128 binary image, accompanied by its period and thickness values. The image is processed through the Input Convolution Block following the standard ResNet pipeline, while the period and thickness parameters are transformed via an Input Linear Block, tiled to match the spatial dimensions of the feature maps, and added after each ResNet Layer Block. This design ensures that these scalar parameters remain integrated throughout processing, guiding the image-based feature extraction. Finally, a Projection Layer maps the combined features to a 64-dimensional latent vector \mathbf{P} .

The spectra encoder (Fig. S2b) takes as input a 58-dimensional concatenated transmission spectrum for x - and y -polarizations, \mathbf{S} , and processes it through an MLP-based architecture. It begins with an Input Linear Block, followed by a Projection Layer that outputs a 64-dimensional latent vector \mathbf{C} , matching the geometry encoder’s latent space. The structures of all encoder blocks are detailed in Fig. S2c.

Zero shot prediction of spectral response

Figure S3a-c illustrates MOCLIP’s zero-shot prediction process of spectral response of a target geometry. The process starts by encoding the target geometry \mathbf{G}_t with the geometry encoder to produce its latent-space representation \mathbf{P}_t (Fig. S3a). Next, MOCLIP generates a set of probe spectra \mathbf{S}_n (Fig. S3b) and encodes each through the spectra encoder to obtain their corresponding latent-space representations \mathbf{C}_n . By computing the cosine similarity between the geometry’s latent vector and each of the probe spectra latent vectors, MOCLIP generates a score vector indicating how closely each probe spectrum matches the target geometry (Fig. S3c). MOCLIP then selects the best-rated spectrum (Fig. S3c, yellow cell) as its prediction. Figure S3d–e presents the Top- k prediction accuracy and precision for zero-shot spectra prediction using the database generation approach, respectively.

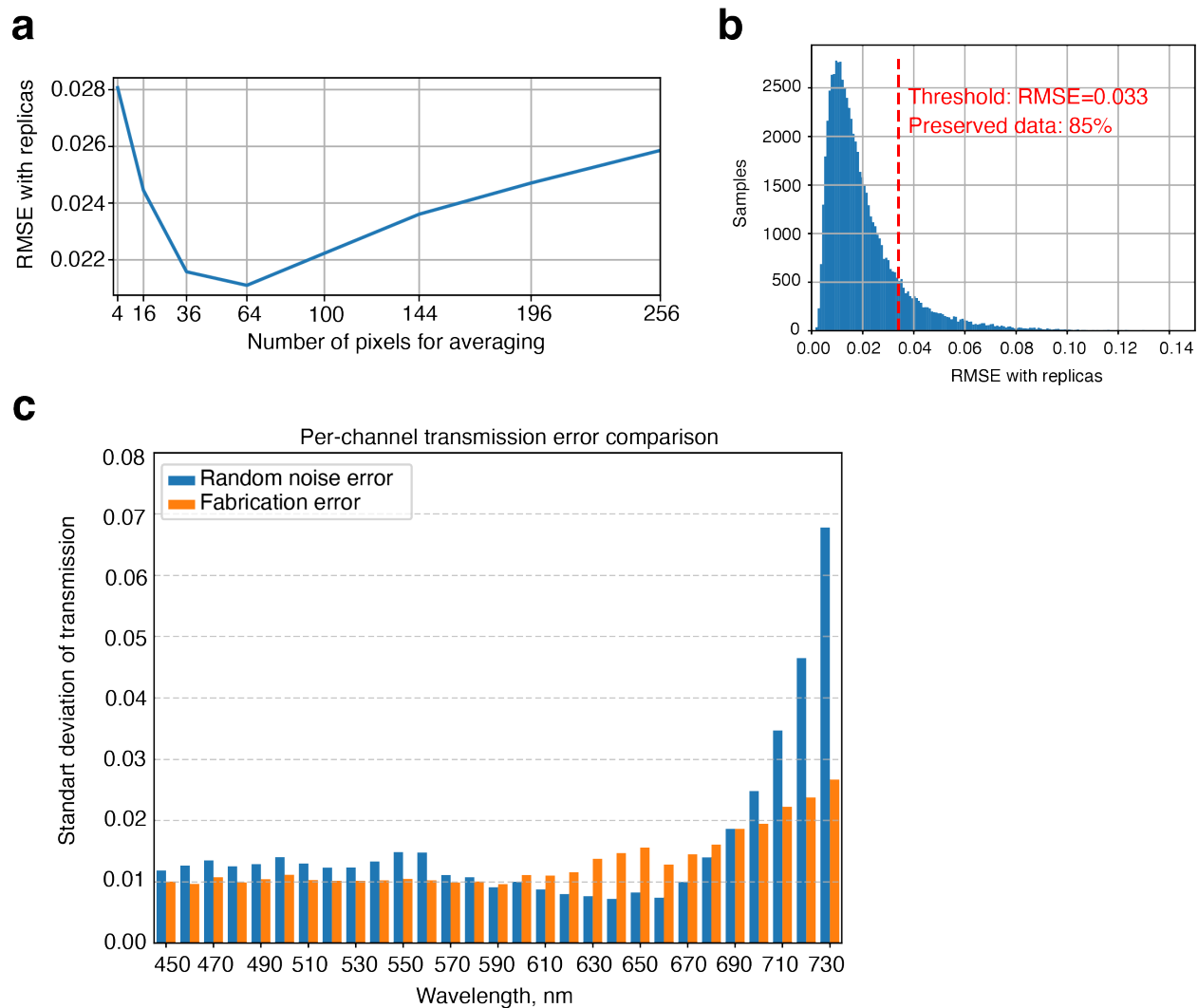


Figure S1: **Measurement error analysis.** **a.** RMSE between original and replicated metasurface spectra as a function of the number of averaged pixels. Averaging over the central 8×8 (64) pixels yields the lowest deviation of 0.021. **b.** RMSE distribution between original and replicated spectra for quality control. **c.** Wavelength-dependent random and fabrication errors, σ_{rand} and σ_{fab} .

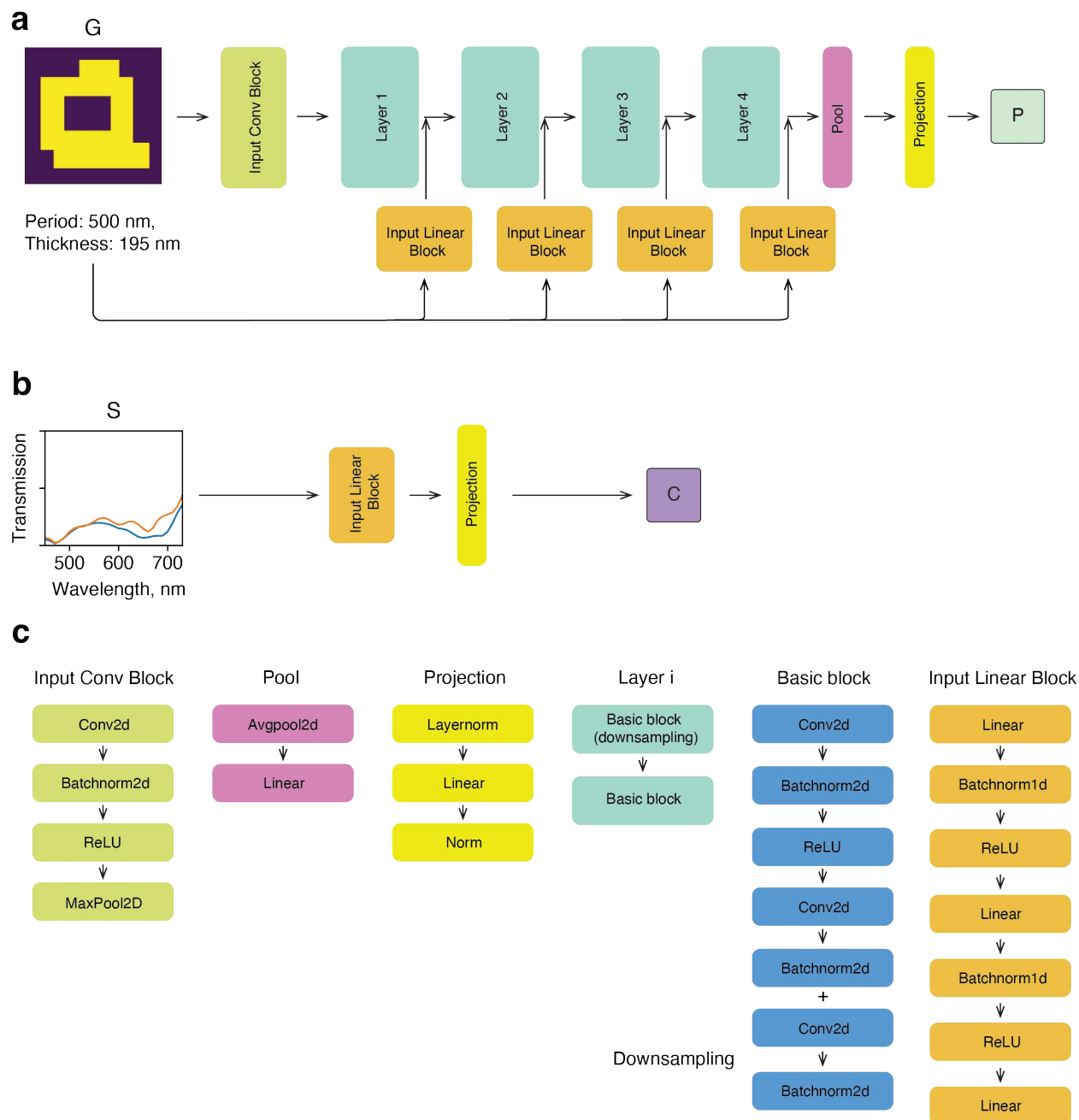


Figure S2: **MOCLIP architecture**. **a**. Geometry encoder architecture based on ResNet. **b**. Spectra encoder architecture based on MLP. **c**. Structure of individual network blocks.

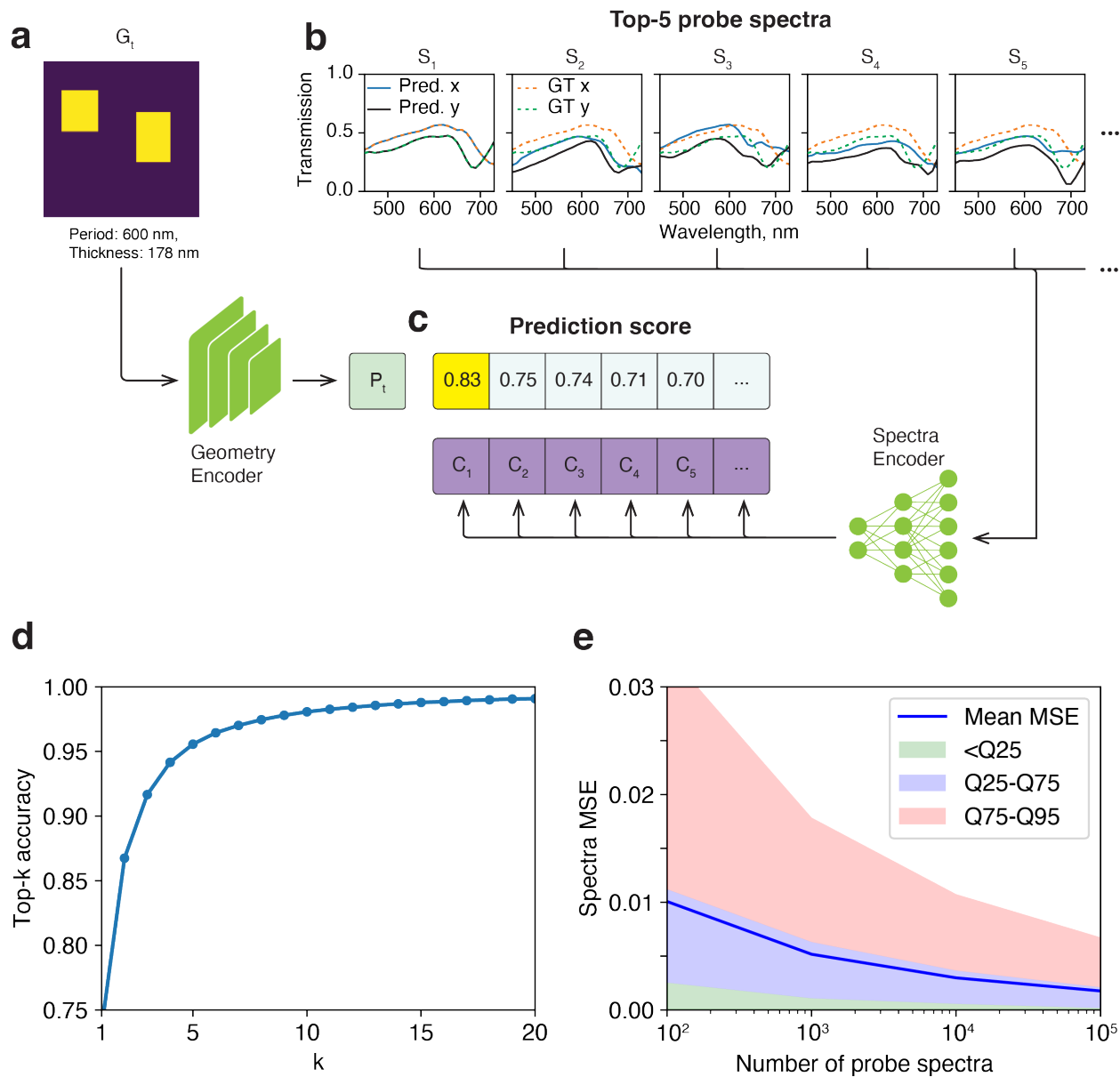


Figure S3: **Zero-shot prediction.** **a.** Target geometry encoding into a latent vector. **b.** Encoding of probe spectra, including the ground truth, into latent vectors. **c.** Similarity score vector between the target geometry and the candidate spectra latent vectors. The yellow cell indicates the best matching score for the predicted spectrum. **d.** Top-k accuracy for the test dataset. **e.** Statistical distribution of the MSE between the spectra corresponding to the target geometry and predicted spectra as a function of the number of probe spectra. The shaded bands indicate quantile regions, and the solid line indicates the mean.